Segmented Control of Selenization Environment for High-Quality Cu2ZnSn(S,Se)4 Films Toward Efficient Kesterite Solar Cells

Yue Jian, Litao Han, Xiangrui Kong, Tianliang Xie, Dongxing Kou, Wenhui Zhou, Zhengji Zhou, Shengjie Yuan, Yuena Meng, Yafang Qi, et al.

Segmented Control of Selenization Environment for High-Quality $Cu_2ZnSn(S,Se)_4$ Films Towards Efficient Kesterite Solar Cells

Yue Jian[1,2,3], Litao Han[1,], Xiangrui Kong[1], Tianliang Xie[1], Dongxing Kou[1], Zhengji Zhou[1], Shengjie Yuan[1], Guangxing Liang[2,*], Xianghua Zhang[3], Zhi Zheng[4] and Sixin Wu[1,*]*

Y. Jian, L.T. Han, X.R. Kong, T.L. Xie, D.X. Kou, Z.J. Zhou, S.J. Yuan, G.X Liang, X.H. Zhang, Z. Zheng, S.X. Wu

[1]Key Laboratory for Special Functional Materials of MOE, National & Local Joint Engineering Research Center for High-efficiency Display and Lighting Technology, Collaborative Innovation Center of Nano Functional Materials and Applications, School of Materials, Henan University, Kaifeng, 475004, China.

Y. Jian, G.X. Liang

[2]Shenzhen Key Laboratory of Advanced Thin Films and Applications, College of Physics and Optoelectronic Engineering, Shenzhen University, Shenzhen, 518060, China.

Y. Jian, X.H. Zhang

[3]CNRS, ISCR (Institut des Sciences Chimiques de Rennes), UMR 6226, Université de Rennes, Rennes, F-35000, France.

Z. Zheng

[4]Key Laboratory of Micro-Nano Materials for Energy Storage and Conversion of Henan Province, Institute of Surface Micro and Nano Materials College of Chemical and Materials Engineering, Xuchang University, Xuchang, 461000, China.

E-mail: hlt@henu.edu.cn, wusixin@henu.edu.cn, lgx@szu.edu.cn.

Abstract

High-crystalline-quality absorbers with fewer defects are crucial for further improvement of open-circuit voltage (V_{OC}) and efficiency of $Cu_2ZnSn(S,Se)_4$ (CZTSSe) solar cells. However, the preparation of high-quality CZTSSe absorbers remains challenging due to the uncontrollability of the selenization reaction and the complexity of the required selenization environment for film growth. Herein, we propose a novel segmented control strategy for the selenization environment, specifically targeting the evaporation area of Se, to regulate the selenization reactions and improve the absorber quality. The large evaporation area of Se in the initial stage of the selenization process provides a great evaporation and diffusion flux for Se, which facilitates rapid phase transition reactions and enables the attainment of a single-layer thin film. The reduced evaporation area of Se in the later stage creates a soft-selenization environment for grain growth, effectively suppressing the loss of Sn and promoting element homogenization. Consequently, the mitigation of Sn-related deep level defects on the surface and in the bulk induced by element imbalance is simultaneously achieved. This leads to a significant improvement in non-radiative recombination suppression and carrier collection enhancement, thereby greatly enhancing the V_{OC}. As a result, the CZTSSe device delivers an impressive efficiency of 13.77% with a low V_{OC} deficit.

Keywords: CZTSSe solar cell, segmented control, selenization reaction, evaporation area of Se, deep-level defects

1. Introduction

$Cu_2ZnSn(S,Se)_4$ (CZTSSe) solar cells are regarded as one of the most promising photovoltaic materials due to their abundant raw material reserves, low toxicity, high light absorption coefficient, and adjustable direct band gap.[1-4] Extensive research has been conducted on CZTSSe solar cells over the years, resulting in a power conversion efficiency (PCE) of 14.9% using the solution method, further demonstrating the tremendous potential of these materials.[5] Nevertheless, in comparison to its counterparts such as $Cu(In,Ga)Se_2$ (CIGS, 23.4%)[6] and CdTe (22.4%),[7] CZTSSe faces a significant limitation in achieving higher efficiency due to its large open-circuit voltage deficit ($V_{OC,def}$), primarily attributed to undesirable morphology and abundant deep-level defects within the absorber layer.[8-11]

The fabrication of high-quality CZTSSe absorbers encounters certain challenges due to the uncontrolled selenization reaction, intricate crystallization process, and multiple constituent elements.[12-14] Firstly, the selenization reaction involves the phase transformation of CZTS to CZTSSe in a selenium atmosphere, which is primarily regulated by various factors such as selenization temperature, initial Se content, Se partial pressure, furnace pressure, volatilization rate of Se vapor, and so on.[15] Uncontrolled reaction pathways can lead to the formation of binary and ternary phases, resulting in a substantial number of defects in the films.[1] Secondly, the crystallization process encompasses two stages: reaction-controlled nucleation and diffusion-controlled grain growth, each with distinct Se atmosphere requirements.[16, 17] The emergence of multi-layer structures resulting from undesirable crystallization patterns can lead to considerable nonradiative recombination at the interface.[18-20] Thirdly, cations with different activities exhibit different volatilization and migration rates during grain growth, leading to the loss and inhomogeneous distribution of elements in the film. The imbalance of the local chemical environment thus exacerbates the proliferation of deep-level-point defects.[21-23] Given all of this, precise control and optimization of the selenization process are imperative for achieving high-crystalline-quality CZTSSe films with low detrimental point defects.

To promote crystallization and suppress defects, multiple strategies have been employed to optimize the selenization process, such as regulating furnace pressure,[1] implementing two-step annealing,[24-26] introducing soft-selenization,[23] utilizing H_2Se atmosphere,[27] employing Se&LiF[28] or Se&SnS[29] co-selenization, among others. In particular, two-step annealing has demonstrated significant advantages in alleviating intrinsic defects and secondary phases by providing ideal selenization atmospheres at different stages of selenization. Nevertheless, ensuring the reproducibility of high-quality CZTSSe films remains a challenge due to the difficulty in accurately controlling the Se atmosphere within the narrow and semi-closed

graphite box by using external selenization parameters.[15] Comparatively, optimizing solid Se inside the graphite box can directly control the Se vapor concentration and the selenization reaction but has received relatively little attention. Currently, most studies only focus on providing sufficient initial Se to achieve saturated Se pressure while overlooking other characteristics of Se,[30, 31] which presents several limitations. Firstly, excessive use of Se may result in the rapid migration of cations during the film growth stage, leading to an imbalance in the chemical environment and the generation of a large number of defects. Secondly, the volatilization, transport, and diffusion rates of Se relied on content are spontaneous and uncontrollable; thus timing and content of its entry into the film for reaction remain uncontrolled as well. Consequently, it is impossible to provide segmented control over different stages of grain growth during selenization by solely manipulating the amount of Se content alone. Therefore, more effective regulation strategies are urgently required to exert control over the selenization reaction for obtaining high-quality CZTSSe absorbers.

In this study, we have introduced a novel segmented control strategy to regulate the selenization reaction by manipulating the evaporation area of Se. Specifically, we provide a relatively large evaporation area of Se in the early stage of selenization to achieve high evaporation and diffusion rates of Se, which has been demonstrated to be advantageous for enhancing the crystallinity of the absorber in our previous research.[32] Subsequently, the evaporation area of Se is reduced to introduce a soft-selenization environment, suppressing the Sn loss and promoting the homogenization of elements. This meticulous design simultaneously optimizes CZTSSe grain growth, reduces film surface potential fluctuations, and enhances defect dynamics by minimizing deep-level defects and defect-assisted non-radiative recombination. Through further optimization, we have achieved high-performance CZTSSe solar cells exhibiting a photoelectric conversion efficiency of 13.77% along with an impressive V_{OC} of 526 mV. This work provides a new approach for comprehensively understanding and precisely controlling the selenization process, thus advancing kesterite solar cell development towards higher efficiencies.

2. Results and discussion

As demonstrated in our published work,[32] regulating the evaporation area of Se during the early stage of selenization can provide a variety of Se atmospheres for grain growth, thereby controlling the nucleation position and crystallization mode of the CZTSSe films. Therefore, the appropriate evaporation area of Se (245 mm^2) can provide relatively large evaporation, transport, and diffusion rates of Se in the graphite box, thus improving the reactivity of Se, promoting the rapid formation of the kesterite phase and obtaining a large-grain spanning

monolayer (**Figure S1**, Supporting Information). However, during the later stage of selenization (grain growth stage), the extensive evaporation area of Se (245 mm^2) induces rapid upward diffusion of cations from the bottom of the film, consequently resulting in an accelerated rate of grain growth. Thus, a film with a non-uniform distribution of cations and a rough surface is obtained, which gives rise to a significant number of point defects. To promote the homogenization of cationic elements and create a favorable local chemical environment for CZTSSe growth, which is determined by the diffusion process involving Se, we implement segment control during late-stage selenization and introduce a soft-selenization process by reducing the evaporation area of Se during the film growth stage (as shown in **Figure 1a-c**). The optimal timing for the initiation of soft-selenization, i.e., when the evaporation area of Se is reduced from 245 mm^2 to 147 mm^2, is meticulously checked by comparing the performance of the devices within a time range of 6 to 13 minutes (**Figure S1-S4, Supporting Information**). The time to introduce soft-selenization starts from 6 min because the grains have just begun to appear on the surface film when the selenization time is 5 minutes (**Figure S1**). Remarkably, the devices subjected to soft-selenization exhibit excellent performances, among which the solar cells with soft-selenization starting from 11 min demonstrate the best. Next, an in-depth investigation into the optimal Se evaporation area ranging from 245 mm^2 to 49 mm^2 with a step of 49 mm^2 is conducted while keeping the starting time of soft-selenization fixed at 11 minutes. Device performance comparisons are made (**Figure S5-S7, Supporting Information**), revealing that champion efficiency is achieved under specific selenization conditions: selenization for 11 minutes with a Se evaporation area of 245 mm^2 followed by an additional selenization period lasting for another 5 minutes using a reduced Se evaporation area of only 98 mm^2. To gain a more comprehensive understanding of the influence of segmented control over the selenization environment on CZTSSe solar cells, our investigation specifically focuses on characterizing the modified sample (referred to as EA-B) subjected to soft-selenization, as well as a reference sample (designated as EA-245).

The EA-B cells demonstrate superior performance compared to the EA-245 cells (**Figure 1d**), exhibiting a significantly improved average power conversion efficiency (PCE) (from 11.30% to 12.60%, without MgF_2 anti-reflection coating), resulting from the greatly boosted average fill factor (FF) (from 62.00% to 65.70%) and open-circuit voltage (V_{OC}) (from 469 to 489 mV). The most efficient solar cell achieves an efficiency of 12.76%, with V_{OC} of 492.0 mV, short circuit current density (J_{SC}) of 39.40 $mA \cdot cm^{-2}$, and *FF* of 65.8%. However, as depicted in **Figure 1e** and **Table 1**, the highest efficiency attained by the EA-245 device is recorded as being at a value of only 11.73%. Above 1% efficiency increment is achieved by the

segmented control of the selenization environment as a result of the improvement in V_{OC} and FF. This can be attributed to the provision of a more favorable chemical environment for CZTSSe absorber growth, thereby mitigating internal defects. The EA-B device is subsequently annealed at a low temperature of 90 ℃ for 6 h to further enhance its performance. The optimal efficiency has been optimized again from 12.76% to 13.77%, with V_{OC} of 526.0 mV, J_{SC} of 39.34 mA·cm^{-2}, and FF of 66.54%, as shown in **Figure 1f**. It has been reported that heat treatment of cells plays a crucial role in enhancing the V_{OC} by optimizing the built-in potential and carrier concentration within the p-type or n-type regions.[2] In comparison with other state-of-the-art kesterite solar cells that exhibit efficiencies beyond 12% (**Table 2**), our cells demonstrate cutting-edge performance with a low V_{OC} deficit (E_g/q-V_{OC}) of 0.534 V and a large V_{OC} gain (V_{OC}/V_{OC}^{SQ}) of 0.64, which is comparable to the record values for CZTSSe (i.e., certified PCE of 14.9% with V_{OC}/V_{OC}^{SQ} of 0.66 and E_g/q-V_{OC} of 0.525 V). The FF below 70% is the main factor limiting the further improvement of the 13.77% efficiency in this work. This issue can be attributed to the high series resistance between each layer of the device, such as the CZTSSe/CdS, Mo/CZTSSe interface, ZnO/ITO interface, Ag grid electrodes, and so on. The incorporation of a modification layer at the interface can facilitate the efficient transfer and collection of charge carriers between functional layers, further improving the FF and thus pushing PCE to 15%.[33, 34] In addition, the major advantage exhibited by our developed cell is the relatively high J_{SC}, which is because the segmented control of selenization can accurately control the reaction rate between precursor film and Se, and effectively regulate the grain growth process of the CZTSSe absorber, thus obtaining a high-crystalline-quality absorber without voids and small-grain layer. The popularization of this process may also improve the J_{SC} of the solar cells in other research groups, thereby elevating the efficiency of CZTSSe to new heights.

To establish a correlation between device performance and the quality of the CZTSSe absorber, which is improved by the segmented control of the selenization environment, the morphological structures of the films are identified using a scanning electron microscope (SEM) (**Figure 2a-b**). The EA-B and EA-245 films both exhibit a large grain structure with no small grains and voids at the bottom. However, compared to EA-245 film with a relatively rough surface, sample EA-B displays a compact, smooth, and uniform morphology. To elaborate further, the various values of the root mean square (RMS) roughness extracted from atomic force microscope (AFM) data are analyzed (**Figure 2c-d**). The RMS roughness of the EA-B film (67 nm) is found to be smaller than that of the EA-245 film (81 nm), consistent with the SEM results, indicating that film EA-B possesses a smoother surface relative to sample EA-

245. Typically, increased surface roughness will result in incomplete CdS coverage on the absorber layer, which augments the shunt path between the CZTSSe absorber and the window layer. Conversely, a smooth surface facilitates the dense adsorption of CdS, thereby enhancing the quality of the heterojunction and reducing the carrier recombination at the P-N heterojunction.[39] Furthermore, the effects of soft-selenization on nanoscale electronic properties and defect properties of CZTSSe absorbers are explored. **Figure 2e-f** presents Kelvin probe force microscopy (KPFM) images of EA-245 film and EA-B film, where the color contrast in the contact potential difference (CPD) maps represents the different values of the CPD obtained from KPFM signals. As can be seen from the CPD maps, both films appear brighter at the grain boundaries (GBs) and darker within grain internals (GIs), indicating higher potential at GBs compared to GIs.[29, 40, 41] The variation of CPD with topography is investigated by acquiring line profiles along the designated regions, as illustrated in **Figure 2g-h**. The CPD profile of sample EA-245 is -483.39 ± 40.01 mV with GBs exhibiting a higher surface potential than GI due to possible segregation of Cu_{Sn}, Zn_{Sn}, and other deep-level point defects at the GBs.[42] Such defect segregation often leads to a larger potential distribution between GBs and GIs.[43] The EA-B film displays a smooth CPD profile with a reduced average CPD of -597.75 ± 37.11 mV compared to the EA-245 film, demonstrating a narrow distribution in the CPD profile. In the case of the CIGS system, a wider distribution of the CPD profile between GI and GB is reported to be advantageous as it facilitates the formation of a local electrostatic field and enhances the separation and transmission of the charge carriers, thereby improving the FF and V_{OC}.[44] In contrast to CIGS, CZTSSe is more susceptible to the generation of detrimental point defects such as Cu_{Sn} and Zn_{Sn} due to its nonstoichiometric composition, local chemical environment imbalance, and lower formation energy. These detrimental defects, localized at grain boundaries, act as recombination centers for charge carriers, which has potential negative hazards to device efficiency. For this reason, the CPD variations observed in CZTSSe cannot be interpreted in a similar way to CIGS. The smooth potential variations and narrow distribution of CPD detected in EA-B film are attributed to the passivation of deep-level defects through the implementation of a soft-selenization process,[45] which is further supported by DLTS analysis discussed subsequently.

The aforementioned results suggest that implementing soft-selenization, achieved by reducing the evaporation area of Se during the later stage of selenization, not only enhances the surface smoothness of the film but also effectively passivates the deep-level point defects. The enhancement of film quality is closely associated with the soft-selenization conditions, which fundamentally modify the dynamics required for subsequent reactions and interdiffusion of

elements during CZTSSe growth. Energy dispersive spectrometer (EDS) analysis is employed to investigate element diffusion in the film, as depicted in **Figure 3a-b**. Cu and Zn are found to exhibit slight enrichment in the upper layer of EA-245 film, while Ag displays an even distribution. Surprisingly, all cations are uniformly distributed in EA-B film. **Table 3** presents atomic content identified from EDS data for both EA-B and pristine EA-245 films. Compared to the EA-245 film, the EA-B film possesses a relatively suitable Cu-poor and Zn-rich composition, which has been widely acknowledged for its positive impact on efficiency. To further explore how soft-selenization regulates the element distribution and cation ratios, we subsequently devise a semi-selenization process for both sample types to investigate the local chemical environment and element migration upon the introduction of soft-selenization. The selenization process terminates upon reaching a duration of 13 minutes, as illustrated in **Figure S10**. The phase composition of semi-selenized EA-B is indistinguishable from that of EA-245. All the semi-selenized samples are exclusively composed of CZTSSe, as identified by the XRD patterns and Raman spectra (**Figure S11**). No discernible secondary phases are observed in the absorber layer, indicating completion of CZTSSe synthesis within 11 minutes of selenization and entry into the grain-growth stage. However, there exist significant disparities in local chemical environments and element diffusion distributions between EA-B and EA-245 films. The proportion of metal elements in the upper, middle, and lower regions of every CZTSSe absorber is subjected to statistical analysis, wherein three points are sampled from each region and averaged (**Figure S12** and **Table S3**, Supporting Information). As illustrated in **Figure 3c-d**, the (Cu+Ag)/(Zn+Sn) ratio remains above 0.9 at the upper region of the semi-selenized EA-245 film but decreases below 0.8 towards the bottom region. This Cu gradient can be attributed to its faster migration rate from bottom to top during the grain growth stage compared with Zn and Sn.[46] The ratio also exceeds the feeding ratio (0.76) due to the Sn loss caused by the formation and escape of gaseous $Sn(S,Se)_x$ from the film during high-temperature selenization.[47] The Sn/Zn ratio increases with the depth of the film but always remains below the feeding ratio value (0.85), suggesting potential Sn loss from CZTSSe film with more pronounced surface depletion than its bottom region. After the completion of selenization (16 min), the distribution of metal elements becomes increasingly heterogeneous and displays pronounced gradients (**Figure 3e-f**). The (Cu+Ag)/(Zn+Sn) ratio on the top and the Sn/Zn ratio even exceed 1, which is much higher than the stoichiometric ratio. Contrastingly, the distribution of elements exhibits greater uniformity at various depths of the semi-selenized EA-B film, with the (Cu+Ag)/(Zn+Sn) and Sn/Zn ratios consistently maintained within the range of 0.85-0.9 and 0.75-0.8, respectively. According to theoretical calculations, the formation

energy of the intrinsic defect cluster reaches its maximum value when Cu/(Zn+Sn) is 0.8 and Sn/Zn is 0.83.[48, 49] Furthermore, no significant alterations are observed in the element distribution or metal cation ratios upon completion of the selenization process. This indicates that reducing the evaporation area of Se during the later stage of selenization can establish a mild environment for enhancing the uniform distribution of elements in the film, while simultaneously suppressing Sn loss. Considering that the growth of CZTSSe film predominantly occurs from top to bottom, it can also be inferred that the surface CZTSSe phase in the case of EA-245 primarily develops under relatively unfavorable Cu-rich, Zn-rich, and Sn-poor conditions. Correspondingly, the lower region of the EA-245 film contains a relatively Cu-poor, Zn-poor, and Sn-rich environment, which may contribute to the generation of numerous Sn-related deep-level defects.

A schematic diagram is proposed to illustrate the crystal growth mechanism and defect formation mechanism in the selenization process (**Figure 4**). The reaction-nucleation stage lasts approximately 2 min, while the subsequent diffusion-controlled grain growth stage continues until the completion of selenization, which is crucial for the crystallinity and defect properties. During the initial stage of selenization, the Se evaporation area (245 mm^2) is strategically designed to provide a moderate Se flux and reaction rate, ensuring that nucleation predominantly occurs on the surface of both EA-245 and EA-B films.[32] As Se vapor continuously permeates into the film, the CZTSSe nuclei grow into small grains and then gradually mature into large grains. This growth and ripening process requires the support of the underlying cations. For the EA-245 film, the unaltered evaporation area of Se during the grain growth stage provides a large Se flux, resulting in the rapid upward migration of cations. Cu, followed by Zn, is more inclined to migrate from the bottom to the surface of the film compared to Sn, thereby creating a Cu-rich and Zn-rich chemical environment for the growth of surface grains.[46, 50] It has been reported that liquid Cu-Se phases are easily formed by Cu and Se interaction as necessary diffusion paths for cations, leading to accelerated grain growth with uneven surfaces. The rough surface leads to the enrichment of deep-level defects, such as Cu_{Sn} and Zn_{Sn}, at grain boundaries. For the EA-B film with a soft-selenization, the evaporation area of Se in the grain growth stage is reduced to moderate the rate at which Se diffuses into the film. In this way, the rapid upward migration of Cu and Zn is inhibited and the cation distribution becomes homogenized. Meanwhile, this chemical environment (non-Cu-rich surface) inhibits the violent growth of grains on the surface, so a relatively smooth surface is obtained.

The non-uniform distribution of cations will also result in variations in the chemical environment within the film, leading to a significant number of cation disorders and defect

proliferation. To investigate the influence of the local chemical environment on the electronic quality of the CZTSSe absorber, we analyze the defect formation mechanism by studying ion coordination. The electronic Octet Rule, in which each anion is coordinated by four cations that donate eight electrons to neighboring anions, is employed within the ionically bonded CZTSSe matrix. The XPS profiles are performed on all the semi-selenized and fully-selenized films to confirm the chemical states of cations. The binding energies of, Ag 3d, Cu 2p, Zn 2p, Sn 3d, and Se 3d for both semi-selenized films are found to be almost identical to those of fully selenized EA-B and EA-245 films (**Figure S13**). Cu, Zn, Sn, and Se have been represented as 1+, 1+, 2+, 4+, and 2-, respectively. For the semi-selenized EA-245 at its top region with a Cu-rich, Zn-rich, and Sn-poor environment (high Cu/(Zn+Sn) and low Sn/Zn ratios), it is possible that some Se^{2-} anions coordinate with two Cu^{1+} ions and two Zn^{2+} ions while some Sn sites may even be occupied by Zn^{2+} or Cu^{1+}, as depicted in Figure **4b**. This local chemical environment enhances the probability of Zn_{Sn} and Cu_{Sn} defects generation. Currently, this film with ion coordination deviating from the electronic Octet Rule is not electrically neutral, as these defects are P-type and negatively charged, such as Zn_{Sn}^{2-}. To maintain electrical neutrality, correspondingly, the composition of Cu-poor, Zn-poor, and Sn-rich at the bottom leads to some Se^{2-} being coordinated by two Sn^{4+}, one Cu^{+} and one vacancy, which increases the possibility of forming N-type Sn_{Zn} defects usually with positive charges. These deep-level Sn-related defects are considered effective nonradiative recombination centers, leading to severe electrostatic potential fluctuations and endangering minority carrier lifetime.[51, 52] In contrast, for the EA-B film, the evenly distributed and favorable composition of Cu-poor, Zn-rich, and Sn-poor enables Se^{2-} to coordinate with one Sn^{4+}, one Zn^{2+}, one Cu^{+} cation, and one vacancy throughout the film. That is to say, compared to the EA-B film, the detrimental deep-level Sn-related defects are effectively suppressed in the EA-B sample and more benign shallow acceptor V_{Cu} are formed, which contributes to the p-type conductivity.[53]

According to the aforementioned results, reducing the evaporation area of Se during the later stage of selenization yields two favorable outcomes: 1) Enhanced surface smoothness of the EA-B film, thereby passivating defects at grain boundaries and improving the P-N heterojunction. 2) Suppression of deep-level Sn-related defects within the absorber and acquisition of more beneficial shallow-level defects. To gain a better understanding of how these improvements enhance cell performance, we conducted external quantum efficiency (EQE) spectra testing on both EA-B and EA-245 devices, as depicted in **Figure 5a**. The significant enhancement in the short wavelength range of 500-600 nm for the EA-B solar cell suggests an improved carrier collection efficiency at the CZTSSe/CdS heterojunction. The

bandgap (E_g) of the EA-B and EA-245 devices are also extracted from EQE spectra, which are 1.055 and 1.062 eV respectively (**Figure 5b**). The reduction of E_g naturally contributes to the improvement in J_{SC} improvement, while it is unfavorable for V_{OC}. Urbach band-tail state analysis model can fit the band-tail photon absorption of the EA-245 device and EA-B device, to analyze whether the soft-selenization in the grain growth stage will have an impact on the band-tail state of the CZTSSe solar cell.[54] It has been reported that the Urbach energy parameter (E_u) can be quantified by the attenuation exponent of the device in the long wavelength region above 900 nm.[55] As can be seen from **Figure 5c**, the E_u values for EA-245 device and EA-B device are determined as 44.05 meV and 33.06 meV, respectively. The decrease in E_u for the EA-B device indicates the improved bulk and surface properties resulting from defect suppression. All of these can inhibit carrier recombination in the CZTSSe absorber and further promote the increase of V_{OC}.

The primary recombination pathways in these two types of solar cells are determined by the temperature-dependent current density voltage (J-V-T). As depicted in **Figure 5d-e**, the J-V-T curves are obtained for the EA-245 and EA-B devices by increasing the test temperature from 120 to 320 K under dark conditions. The J-V-T curves of the EA-245 device exhibit weak diode characteristics, while those of the EA-B device still demonstrate superior diode characteristics at low temperatures, indicating a lower transmission barrier in the latter. Moreover, by analyzing the relationship between $1\cdot(KT)^{-1}$ and $Aln(J_0)$, we can calculate the recombination activation energy (E_{ra}) and compare it with the bandgap (E_g) of the solar cells to determine their main recombination pathway. As shown in **Figure 5f**, the E_a values for EA-245 and EA-B devices are determined as 0.821 and 0.941 eV respectively, while the E_g values are found to be 1.055 for the EA-245 device and 1.061 eV for EA-B device correspondingly. When the E_{ra} is close to or equal to the E_g of the absorber, the absorber-neutral region Shockley Reid Hall (SRH) recombination becomes dominant; however, if the E_{ra} is significantly smaller than the E_g, interface-related recombination prevails instead. Therefore, the increase in the E_{ra} value of the EA-B device once again confirms significant improvement in the interfacial defects and interface recombination due to the high-crystalline absorber with a smoother surface.

To assess carrier characteristics and the defect density of CZTSSe absorbers, C-V and DLCP measurements are performed (**Figure 6a-b** and **Table 4)**. The depletion width (W_d) of the EA-B device (0.194 μm) is significantly larger than that of the EA-245 device (0.170 μm), which can be attributed to the improvements in the CdS/CZTSSe heterojunction. An extended W_d offers significant advantages in terms of carrier separation and transportation, thereby enhancing carrier collection efficiency.[56] Generally, C-V exhibits higher sensitivity towards

the interface defects compared to DLCP. The CV response (N_{CV}) encompasses interface defects, bulk defects, and free carriers, while the DLCP result (N_{DL}) solely reflects the correlation between bulk defects and free carriers.[13, 57, 58] Therefore, the disparity between them represents the interface defect density in the devices. The interface defect density of the EA-B device (1.4×10^{15} cm^{-3}) is lower than that of the EA-245 device (2.5×10^{15} cm^{-3}), also indicating a reduction in surface defects in the EA-B absorber due to its enhanced surface morphology. In comparison to C-V analysis, DLCP results (N_{DL}) provide a more accurate evaluation of free carrier density as well as deep-level defect states within CZTSSe absorbers. For EA-245 and EA-B devices, the charge density (N_{DL}, including defects and free carriers) extracted from DLCP are 1.28×10^{16} cm^{-3} and 0.99×10^{16} cm^{-3}. In CZTSSe, the provision of free carriers is typically attributed to shallow acceptor defects like V_{Cu}, which primarily depends on the composition of CZTSSe. Consequently, the reduction in charge density (N_{DL}) observed in the EA-B device may be attributed to the decrease in deep-level defects.

To gain profound insights into the evolution of spatial defects environment, capacitance-mode deep-level transient spectroscopy (C-DLTS) is conducted under dark conditions within a temperature range of 200 K-300 K. The DLTS spectrum is depicted in **Figure 6c**, exhibiting two distinct signal peaks at temperatures of 240 K and 275 K respectively, which correspond to the location and quantity of defects. Arrhenius curves (**Figure 6d**) are employed to identify the defect type and concentration (N_T) in the CZTSSe devices, with detailed parameters listed in **Figure 6e-f** and **Table 5**. The defect activation energy (E_a) represents the spatial distance between the defect level and the valence band, with a greater E_a indicating a deeper position of the defect energy level. According to first-principles calculations, E_a values ranging from 0.25 to 0.38 eV can be assigned to Cu_{Sn} defects while those ranging from 0.4 eV to 1 eV can be ascribed to Sn_{Zn} defects. Therefore, the peak observed near 240 K corresponds to the characteristic Cu_{Sn} defects, while the peak near 275 K represents the characteristic Sn_{Zn} defects. After optimizing the selenization process, lower E_a values for Cu_{Sn} and Sn_{Zn} defects are obtained in device EA-B compared to device EA-245. This indicates that the soft-selenization can enhance the carrier emission rate of Cu_{Sn} and Sn_{Zn} deep-level defects, and improve the collection and separation ability of carriers in the devices, thus increasing the carrier lifetime.[23, 57, 59] The N_T of Cu_{Sn} and Sn_{Zn} defects also decrease from 2.81×10^{14} cm^{-3} and 1.77×10^{14} cm^{-3} to 1.97×10^{13} cm^{-3} and 1.64×10^{13} cm^{-3}, respectively. The reduction in Sn_{Zn} and Cu_{Sn} defect concentrations aligns with previous analysis findings, ascribed to the smaller Se evaporation area during later stages of selenization that stabilizes cation diffusion rates within the absorber layer, thereby creating a more favorable chemical environment for grain growth. This decrease

in Sn_{Zn} defects effectively mitigates band tailing effects and carrier recombination in the absorber layer, leading to improved V_{OC} and PCE.

Next, we performed photoluminescence spectroscopy (PL), transient photocurrent (TPC), and transient photovoltage (TPV) on the EA-245 device and EA-B device. The PL test is employed to determine the surface band gap of the absorber. As depicted in **Figure 6g**, the PL emission peak energy (EPL) of the EA-245 sample is measured to be 1.022 eV, exhibiting a slight reduction of 0.04 eV compared to its corresponding E_g value of 1.061 eV obtained from EQE data. In contrast, for the EA-B sample, there is only a marginal difference of 0.02 eV between the EPL and E_g values, indicating effective suppression of potential fluctuations in the EA-B absorber.[60, 61] Additionally, it should be noted that EA-B film exhibits significantly higher PL intensity. Enhanced PL intensity suggests a reduced concentration of non-radiative recombination centers within the absorber layer, thereby minimizing the carrier capture by defects and prolonging the carrier lifetime.[52] To further investigate the charge transport property of the CZTSSe devices, TPC and TPV measurements are performed. TPC lifetime (τ_{TPC}) represents the charge extraction dynamics in a device (**Figure 6h**).[62-64] The TPC response decreases from 5.54 μs for the EA-245 device to 3.16 μs for the EA-B device, demonstrating faster carrier extraction and transmission in the latter. On the other hand, the TPV lifetime (τ_{TPV}) reflects the charge recombination rate (**Figure 6i**). The TPV response lifetime of the EA-B device (122.2 μs) is three times longer than that of the EA-245 device (37.3 μs), indicating an effective reduction in charge recombination within the former. The charge transport characterization reveals that the EA-B film with better crystallinity, significantly reduces the trap defect density and improves the charge transport in the device.

3. Conclusion

In this work, we have implemented a segmented control strategy for the selenization environment by adjusting the evaporation area of Se to cater to varying Se atmosphere requirements during different stages of selenization. The large evaporation area of Se in the early stage promotes the rapid formation of the kesterite phase and improves crystal growth, while the reduced evaporation area of Se in the subsequent stage introduces a soft-selenization process that optimizes the smoothness of the film surface, facilitates the homogeneous distribution of elements, and alleviates the bulk and interface defects. As a result, we have successfully achieved CZTSSe solar cells with a remarkable device *PCE* of 13.77%. On the whole, our work has contributed to a deeper understanding and precise control over the selenization reaction process. This novel selenization strategy provides a new idea for other workers to synergistically regulate the crystal quality and defects of the absorbers. Regulating

the evaporation area of Se is not limited to two-stage selenization. Moreover, designing more variations in the evaporation area of Se and implementing multi-stage control throughout the entire selenization process may be more helpful in providing a unique selenization atmosphere for different selenization stages, further facilitating the development of CZTSSe solar cells toward higher efficiency.

4. Experimental section

Reagents and materials: thiourea (NH_2CSNH_2, 99%), 2-Methoxyethanol (EGME, 99.8%), cuprous chloride (CuCl, ≥99.95%), and zinc acetate ($Zn(CH_3CO_2)_2$, 99.99%) were obtained from Aladdin Company. Stannic chloride hydrated ($SnCl_4$, 99.998%) was purchased from Macklin Biochemical Technology Co., Ltd. Silver chloride (AgCl, 99.5%) was purchased from Beijing InnoChem Science & Technology Co., Ltd.

Preparation of CZTSSe film and device assembly: The CZTS precursor film was obtained through the solution-spin coating method onto the Mo-coated soda lime glass substrates. Then the precursor film was annealed to obtain the CZTSSe absorber layer. The detailed preparation process of CZTSSe film and device assembly were described in refs.[32]. In this work, the selenization process was continued to optimize, and details of the experiment are in the Supporting information.

Characterization: The morphology and element depth profiles of CZTSSe films were analyzed using a scanning electron microscope (SEM, JSM-7900F) configured with an energy dispersive spectrometer (EDS). The phase structures of the CZTSSe films were characterized using Raman spectrometer (inVia, Renishaw, UK) with an excitation wavelength of 532 nm and X-ray diffraction (XRD, Bruker D8 Advance) operating at 40 mA and 40 kV with a Cu Kα radiation source (λ=1.5406 nm). The Atomic Force microscope (AFM) and Kelvin Probe Force microscope (KPFM) were obtained from the Atomic Force Scanning probe microscope (Dimension lcon, Bruker) with a scanning area of 3×3 μm^2. The XPS measurements were conducted using an AXIS-ULTRA DLD system equipped with a monochromatic X-ray source. All the XPS binding energies were calibrated by C 1s peak (284.80 eV). The external quantum efficiency (EQE) measurements were performed on a Zolix SCS100 QE system equipped with a 150 W xenon light source and a lock-in amplifier. The photocurrent density-voltage (J-V) characteristics were obtained through the digital source meter (Keithley 2400) in conjunction with a solar simulator (Zolix SS150) under standard test conditions, namely AM 1.5G, 100 mW cm^{-2}. The temperature-dependent dark current density-voltage characteristics (J-V-T) and deep-level transient spectroscopy (DLTS) were investigated using an FT-1030 HERA DLTS system with a cryostat controller (JANIS VPF-800). The J-V-T data were collected with

unbiased voltage and at temperatures ranging from 120 K to 320 K in increments of 10 K. DLTS curves were measured within the temperature range of 200 K to 340 K, with a pulse voltage (Vp) of 0.4 V, reverse biased (V_R) of -0.35 V, and pulse width of 10 ms, respectively. The capacitance-voltage (C-V) and drive-level capacitance profiling (DLCP) measurements were conducted using a Keithley 4200A-SCS system. The steady-state photoluminescence (PL) data were acquired by time-correlated single photon counting (TCSPC) (FluoTime 300, PicoQuant Gmbh). The transient photovoltage (TPV) and transient photocurrent (TPC) were investigated using an Agilent B1500A semiconductor characterization system, while the illumination was provided by a monochromatic light-emitting diode (LED) controlled through a functional generator (Agilent 33210A).

Supporting Information

Supporting Information is available from the Wiley Online Library or the author.

Acknowledgments

This work was financially supported by the National Natural Science Foundation of China (62074052, 61974173, 62104061, and 52072327), the Science and Technology Innovation Talents in Universities of Henan Province (21HASTIT023), the Key scientific and technological project of Henan Province (20B480002), and Science and Technology plan project of Shenzhen (20220808165025003) China.

Conflict of Interest

The authors declare no conflict of interest.

Data Availability Statement

The data that support the findings of this study are available from the corresponding author upon reasonable request.

References

[1] J. Zhou, X. Xu, H. Wu, J. Wang, L. Lou, K. Yin, Y. Gong, J. Shi, Y. Luo, D. Li, H. Xin, Q. Meng, *Nat. Energy* **2023**, *8* (5), 526-535.

[2] Z. Su, G. Liang, P. Fan, J. Luo, Z. Zheng, Z. Xie, W. Wang, S. Chen, J. Hu, Y. Wei, C. Yan, J. Huang, X. Hao, F. Liu, *Adv. Mater.* **2020**, *32* (32), 2000121.

[3] F. Liu, Q. Zeng, J. Li, X. Hao, A. Ho-Baillie, J. Tang, M. A. Green, *Mater. Today* **2020**, *41*,

120-142.
[4] A. Wang, M. He, M. A. Green, K. Sun, X. Hao, *Adv. Energy Mater.* **2023**, *13* (2), 2203046.
[5] M. A. Green, E. D. Dunlop, M. Yoshita, N. Kopidakis, K. Bothe, G. Siefer, X. Hao, *Prog. Photovoltaics* **2023**, *31* (7), 651-663.
[6] M. Nakamura, K. Yamaguchi, Y. Kimoto, Y. Yasaki, T. Kato, H. Sugimoto, *IEEE. J. Photovolt.* **2019**, *9* (6), 1863-1867.
[7] W. K. Metzger, S. Grover, D. Lu, E. Colegrove, J. Moseley, C. L. Perkins, X. Li, R. Mallick, W. Zhang, R. Malik, J. Kephart, C. S. Jiang, D. Kuciauskas, D. S. Albin, M. M. Al-Jassim, G. Xiong, M. Gloeckler, *Nat. Energy* **2019**, *4* (10), 837-845.
[8] Y. Gong, Y. Zhang, Q. Zhu, Y. Zhou, R. Qiu, C. Niu, W. Yan, W. Huang, H. Xin, *Energ. Environ. Sci.* **2021**, *14* (4), 2369-2380.
[9] J. Li, J. Huang, F. Ma, H. Sun, J. Cong, K. Privat, R. F. Webster, S. Cheong, Y. Yao, R. L. Chin, X. Yuan, M. He, K. Sun, H. Li, Y. Mai, Z. Hameiri, N. J. Ekins-Daukes, R. D. Tilley, T. Unold, M. A. Green, X. Hao, *Nat. Energy* **2022**, *7* (8), 754-764.
[10] W. Chen, D. Dahliah, G.-M. Rignanese, G. Hautier, *Energ. Environ. Sci.* **2021**, *14* (6), 3567-3578.
[11] U. Farooq, U. Ali Shah, M. Ishaq, J.G. Hu, S. Ahmed, S. Chen, Z.H. Zheng, Z.H. Su, P. Fan, G.X. Liang, *Chem. Eng. J.* **2023**, *451*, 139109.
[12] M. Kumar, A. Dubey, N. Adhikari, S. Venkatesan, Q. Qiao, *Energ. Environ. Sci.* **2015**, *8* (11), 3134-3159.
[13] P. Fan, J. Lin, J. Hu, Z. Yu, Y. Zhao, S. Chen, Z. Zheng, J. Luo, G. Liang, Z. Su, *Adv. Funct. Mater.* **2022**, *32* (45), 2207470.
[14] X. Xu, J. Zhou, K. Yin, J. Wang, L. Lou, M. Jiao, B. Zhang, D. Li, J. Shi, H. Wu, Y. Luo, Q. Meng, *Nat. Commun.* **2023**, *14* (1), 6650.
[15] J. H. Han, S. Rehan, D. G. Moon, A. Cho, J. Gwak, K. H. Yoon, S. K. Ahn, J. H. Yun, Y. J. Eo, S. Ahn, *J. Mater. Chem. A.* **2016**, *4* (17), 6319-6331.
[16] K. Yin, X. Xu, M. Wang, J. Zhou, B. Duan, J. Shi, D. Li, H. Wu, Y. Luo, Q. Meng, *J. Mater. Chem. A.* **2022**, *10* (2), 779-788.
[17] M. Khammar, F. Ynineb, S. Guitouni, Y. Bouznit, N. Attaf, *Appl. Phys. A-Mater.* **2020**, *126* (6), 8.
[18] F. Martinho, S. Lopez-Marino, M. Espíndola-Rodríguez, A. Hajijafarassar, F. Stulen, S. Grini, M. Döbeli, M. Gansukh, S. Engberg, E. Stamate, L. Vines, J. Schou, O. Hansen, S. Canulescu, *ACS. Appl. Mater. Interfaces* **2020**, *12* (35), 39405-39424.
[19] J. Li, J. Huang, J. Cong, Y. Mai, Z. Su, G. Liang, A. Wang, M. He, X. Yuan, H. Sun, C.

Yan, K. Sun, N. J. Ekins-Daukes, M. A. Green, X. Hao, *Small* **2022**, *18* (9), 2105044.

[20] Z. Zhang, L. Yao, Y. Zhang, J. Ao, J. Bi, S. Gao, Q. Gao, M.J. Jeng, G. Sun, Z. Zhou, Q. He, Y. Sun, *Adv. Sci.* **2018**, *5* (2), 1700645.

[21] Y. Qu, G. Zoppi, N. S. Beattie, *Sol. Energy Mater. Sol. Cells.* **2016**, *158*, 130-137.

[22] D. Pareek, T. Taskesen, J. A. Márquez, H. Stange, S. Levcenco, I. Simsek, D. Nowak, T. Pfeiffelmann, W. Chen, C. Stroth, M. H. Sayed, U. Mikolajczak, J. Parisi, T. Unold, R. Mainz, L. Gütay, *Sol. RRL.* **2020**, *4* (6), 2000124.

[23] J. Li, Y. Huang, J. Huang, G. Liang, Y. Zhang, G. Rey, F. Guo, Z. Su, H. Zhu, L. Cai, K. Sun, Y. Sun, F. Liu, S. Chen, X. Hao, Y. Mai, M. A. Green, *Adv. Mater.* **2020**, *32* (52), 2005268.

[24] P. Fan, Z. Xie, G. Liang, M. Ishaq, S. Chen, Z. Zheng, C. Yan, J. Huang, X. Hao, Y. Zhang, Z. Su, *J. Energy Chem.* **2021**, *61*, 186-194.

[25] F. Jiang, S. Ikeda, T. Harada, M. Matsumura, *Adv. Energy Mater.* **2014**, *4* (7), 1301381.

[26] G. Ren, D. Zhuang, M. Zhao, Y. Wei, Y. Wu, X. Li, X. Lyu, C. Wang, Y. Li, *Sol. Energy* **2020**, *207*, 651-658.

[27] D.H. Son, S.H. Kim, S.Y. Kim, Y.I. Kim, J.H. Sim, S.N. Park, D.H. Jeon, D.K. Hwang, S.J. Sung, J.K. Kang, K.J. Yang, D.H. Kim, *J. Mater. Chem. A* **2019**, *7* (44), 25279-25289.

[28] H. Guo, G. Wang, R. Meng, Y. Sun, S. Wang, S. Zhang, J. Wu, L. Wu, G. Liang, H. Li, Y. Zhang, *J. Mater. Chem. A* **2020**, *8* (42), 22065-22074.

[29] Z. Yu, C. Li, S. Chen, Z. Zheng, P. Fan, Y. Li, M. Tan, C. Yan, X. Zhang, Z. Su, G. Liang, *Adv. Energy Mater.* **2023**, *13* (19), 2300521.

[30] C. J. Hages, M. J. Koeper, C. K. Miskin, K. W. Brew, R. Agrawal, *Chem. Mater.* **2016**, *28* (21), 7703-7714.

[31] J. H. Kim, S.Y. Choi, M. Choi, T. Gershon, Y. S. Lee, W. Wang, B. Shin, S.-Y. Chung, *Adv. Energy Mater.* **2016**, *6* (6), 1501902.

[32] Y. Jian, T. Xie, L. Han, L. Cao, L. Wang, W. Zhou, Z. Zhou, D. Kou, Y. Meng, Y. Qi, S. Yuan, S. Wu, *Sol. RRL* **2023**, *7* (9), 2300006.

[33] Y. Zhao, Z. Yu, J. Hu, Z. Zheng, H. Ma, K. Sun, X. Hao, G. Liang, P. Fan, X. Zhang, Z. Su, *J. Energy Chem.* **2022**, *75*, 321-329.

[34] Y. Jian, T. Xie, L. Han, D. Kou, W. Zhou, Z. Zhou, S. Yuan, Y. Meng, Y. Qi, S. Wu, *J. Mater. Chem. C* **2023**, *11* (14), 4634-4644.

[35] S. S. Hegedus, W. N. Shafarman, *Prog. Photovoltaics* **2004**, *12* (2-3), 155-176.

[36] A. D. Collord, H. W. Hillhouse, *Chem. Mater.* **2016**, *28* (7), 2067-2073.

[37] W. Wang, M. T. Winkler, O. Gunawan, T. Gokmen, T. K. Todorov, Y. Zhu, D. B. Mitzi, *Adv. Energy Mater.* **2014**, *4* (7), 1301465.

[38] Y. Gong, Q. Zhu, B. Li, S. Wang, B. Duan, L. Lou, C. Xiang, E. Jedlicka, R. Giridharagopal, Y. Zhou, Q. Dai, W. Yan, S. Chen, Q. Meng, H. Xin, *Nat. Energy* **2022**, *7*, 966-977.

[39] G. Liang, Z. Li, M. Ishaq, Z. Zheng, Z. Su, H. Ma, X. Zhang, P. Fan, S. Chen, *Adv. Energy Mater.* **2023,** *13* (19), 2300215.

[40] Y. Sun, P. Qiu, W. Yu, J. Li, H. Guo, L. Wu, H. Luo, R. Meng, Y. Zhang, S. Liu, *Adv. Mater.* **2021,** *33* (49), 2104330.

[41] Y. Zhao, X. Zhao, D. Kou, W. Zhou, Z. Zhou, S. Yuan, Y. Qi, Z. Zheng, S. Wu, *ACS. Appl. Mater. Interfaces* **2021,** *13* (1), 795-805.

[42] K. Kaur, Nisika, A. H. Chowdhury, Q. Qiao, M. Kumar, *J. Alloys Compd.* **2021,** *854*, 157160.

[43] J. B. Li, V. Chawla, B. M. Clemens, *Adv. Mater.* **2012**, *24* (6), 720-723.

[44] J. Hwang, H. K. Park, D. Shin, I. Jung, I. Hwang, Y.-J. Eo, A. Cho, J. H. Park, S. Song, Y. Cho, J. Gwak, H. S. Jang, W. Jo, K. Kim, *J. Mater. Chem. A* **2023**, *11*, 19546-19555.

[45] S. Kim, J.S. Park, A. Walsh, *ACS Energy Lett.* **2018**, *3* (2), 496-500.

[46] X. Yin, C. Tang, L. Sun, Z. Shen, H. Gong, *Chem. Mater.* **2014**, *26* (6), 2005-2014.

[47] H. Xie, Y. Sánchez, S. López-Marino, M. Espíndola-Rodríguez, M. Neuschitzer, D. Sylla, A. Fairbrother, V. Izquierdo-Roca, A. Pérez-Rodríguez, E. Saucedo, *ACS Appl. Mater. Interfaces.* **2014**, *6* (15), 12744-12751.

[48] S. Chen, A. Walsh, X.G. Gong, S.H. Wei, *Adv. Mater.* **2013**, *25* (11), 1522-1539.

[49] S. Chen, L. W. Wang, A. Walsh, X. G. Gong, S. H. Wei, *Appl. Phys. Lett.* **2012**, *101* (22), 223901.

[50] R. Mainz, B. C. Walker, S. S. Schmidt, O. Zander, A. Weber, H. Rodriguez-Alvarez, J. Just, M. Klaus, R. Agrawal, T. Unold, *PCCP* **2013**, *15* (41), 18281-18289.

[51] J. Li, Z.K. Yuan, S. Chen, X.G. Gong, S.H. Wei, *Chem. Mater.* **2019**, *31* (3), 826-833.

[52] S. Ma, H. Li, J. Hong, H. Wang, X. Lu, Y. Chen, L. Sun, F. Yue, J. W. Tomm, J. Chu, S. Chen, *J. Phys. Chem. Lett.* **2019**, *10* (24), 7929-7936.

[53] A. Walsh, S. Chen, S.-H. Wei, X.-G. Gong, *Adv. Energy Mater.* **2012**, *2* (4), 400-409.

[54] Y. Zhao, S. Chen, M. Ishaq, M. Cathelinaud, C. Yan, H. Ma, P. Fan, X. Zhang, Z. Su, G. Liang, *Adv. Funct. Mater.* **2023**, *34* (8), 2311992.

[55] S. Wang, S. Gao, D. Wang, Z. Jiang, J. Ao, Z. Zhou, S. Liu, Y. Sun, Y. Zhang, *Sol. RRL* **2019**, *3* (1), 1800236.

[56] Y. Zhao, S. Yuan, Q. Chang, Z. Zhou, D. Kou, W. Zhou, Y. Qi, S. Wu, *Adv. Funct. Mater.* **2020**, *31* (10), 2007928.

[57] H. S. Duan, W. Yang, B. Bob, C. J. Hsu, B. Lei, Y. Yang, *Adv. Funct. Mater.* **2013**, *23* (11),

1466-1471.

[58] N. Ahmad, Y. Zhao, F. Ye, J. Zhao, S. Chen, Z. Zheng, P. Fan, C. Yan, Y. Li, Z. Su, X. Zhang, G. Liang, *Adv. Sci.* **2023**, *10* (26), 2302869.

[59] X. Zhao, X. Chang, D. Kou, W. Zhou, Z. Zhou, Q. Tian, S. Yuan, Y. Qi, S. Wu, *J. Energy Chem.* **2020,** *50*, 9-15.

[60] S. Levcenko, J. Just, A. Redinger, G. Larramona, S. Bourdais, G. Dennler, A. Jacob, T. Unold, *Phys. Rev. Appl.* **2016**, *5* (2), 024004.

[61] H. Geng, M. Wang, S. Wang, D. Kou, Z. Zhou, W. Zhou, Y. Qi, S. Yuan, L. Han, Y. Meng, S. Wu, *Adv. Funct. Mater.* **2022**, *33* (3), 2210551.

[62] X. Gan, S. Yang, J. Zhang, G. Wang, P. He, H. Sun, H. Yuan, L. Yu, G. Ding, Y. Zhu, *ACS Appl. Mater. Interfaces* **2019**, *11* (41), 37796-37803.

[63] Q. Gao, S. Yuan, Z. Zhou, D. Kou, W. Zhou, Y. Meng, Y. Qi, L. Han, S. Wu, *Small* **2022**, *18* (39), e2203443.

[64] Q. Chang, S. Yuan, J. Fu, Q. Gao, Y. Zhao, Z. Xu, D. Kou, Z. Zhou, W. Zhou, S. Wu, *ACS Appl. Mater. Interfaces* **2022**, *14* (4), 5149-5158.

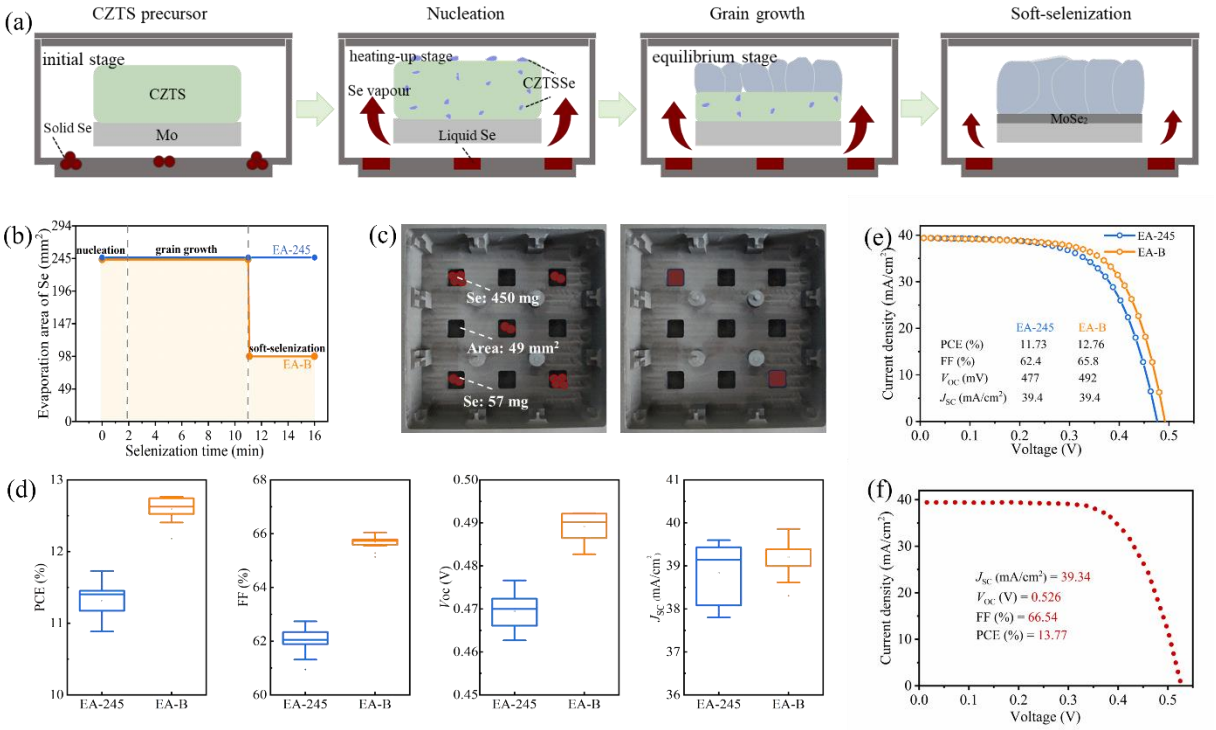

Figure 1. a) The segmented control of selnization environment. The large red arrow represents a high volatilization and diffusion flux of Se in the early stage of selenization process, while the small arrow indicates a low flux in the later stage. b) Se evaporation area profiles of the reference sample EA-245 and sample EA-B with modified growth process. c) Se placement in the graphite box for achieving the soft-selenization condition of EA-B. Selenium is present in all five holes before selenization, with a total evaporation area of 245 mm^2. When selenization time reaches 11 min, only two holes contain selenium, with a total evaporation area of 98 mm^2. More detailed analysis in **Supporting Information S3**. d) Statistical of photovoltaic parameters of EA-245 and EA-B devices without MgF_2 antireflection layers. e) J-V curves of champion solar cells for EA-245 and EA-B. f) J-V curve of the EA-B device after annealing.

Table 1. Summary of the photovoltaic and diode parameters of the best solar cells from EA-245 and EA-B. The diode parameters are extracted based on the J-V curves using the Site's methods (**Figure S8**, Supporting Information).[35]

Sample	V_{OC} [mV]	J_{SC} [mA·cm^{-2}]	FF [%]	PCE [%]	R_s [Ω·cm^2]	R_{sh} [Ω·cm^2]	G_{sh} [mS·cm^2]	A
EA-245	477	39.4	62.43	11.73	0.54	976	1.02	1.47
EA-B	492	39.4	65.84	12.76	0.50	1152	0.87	1.29

Table 2. Comparison between the photovoltaic characteristics of state-of-the-art kesterite solar cells and the solar cell developed within this work. The V_{OC} deficit compared to the Shockley-Queisser (S-Q) limit (V_{OC}/V_{OC}^{SQ}) is calculated using Collord's method.[36] The value of E_g is obtained from the EQE data (see **Figure S9, Supporting Information**).

Cell	PCE [%]	J_{SC} [mA·cm^{-2}]	V_{OC} [mV]	FF [%]	E_g [eV]	V_{OC}/V_{OC}^{SQ}	E_g/q-V_{OC} [mV]	Area [cm^2]	Ref.
CIGSSe (Idemitsu)	23.4	39.6	734	80.4	1.08	0.88	346	1.04	[6]
CZTSSe (IBM)	12.6	35.2	513	69.8	1.13	0.59	617	0.42	[37]
CZTSSe (NJUPT)	13.0	33.7	529	72.9	1.11	0.60	581	0.11	[38]
CZTSSe (IoP/CAS)	14.9	36.9	555	72.5	1.08	0.66	525	0.27	[5]
CZTSSe (This work)	13.77	39.3	526	66.5	1.06	0.64	534	0.11	

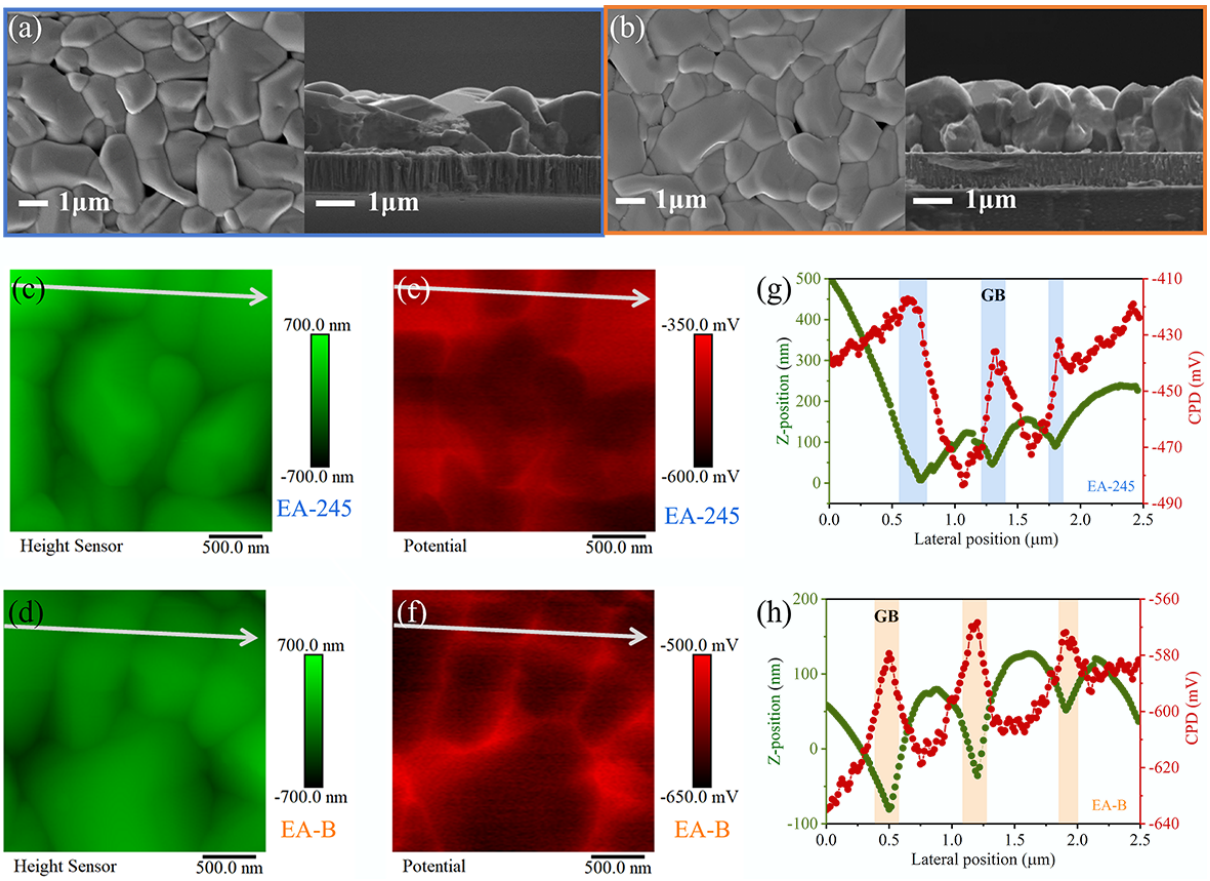

Figure 2. Top-view and cross-sectional SEM images of a) EA-245 absorber and b) EA-B absorber. c–d) AFM scanning surface topography. e–f) KPFM data depicting the topography. g–h) Z vs. CPD profile along the marked region for EA-B and EA-245 film.

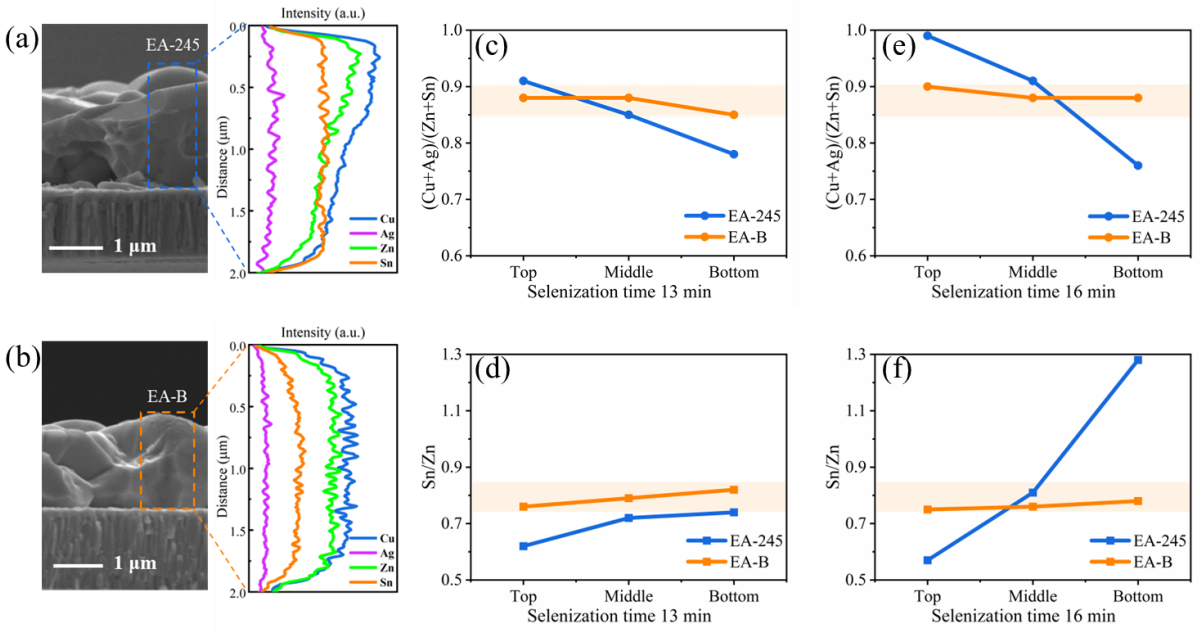

Figure 3. EDS element maps of a) the EA-245 absorber and b) the EA-B absorber. c) (Cu+Ag)/(Zn+Sn) and d) Sn/Zn of the different absorbers with 13 minutes of selenization. e) (Cu+Ag)/(Zn+Sn) and f) Sn/Zn of the different absorbers with 16 minutes of selenization.

Table 3. EDS composition of fully-selenized EA-B and EA-245 CZTSSe films. M represents the total amount of cations.

Sample	Cu [at%]	Ag [at%]	Zn [at%]	Sn [at%]	S [at%]	Se [at%]	(Cu+Ag) /(Zn+Sn)	Sn/Zn	(Se+S)/M
EA-245	22.1	0.7	15.0	9.2	3.0	50.0	0.94	0.61	1.12
EA-B	22.6	0.9	14.8	12.7	2.7	46.3	0.86	0.87	0.96

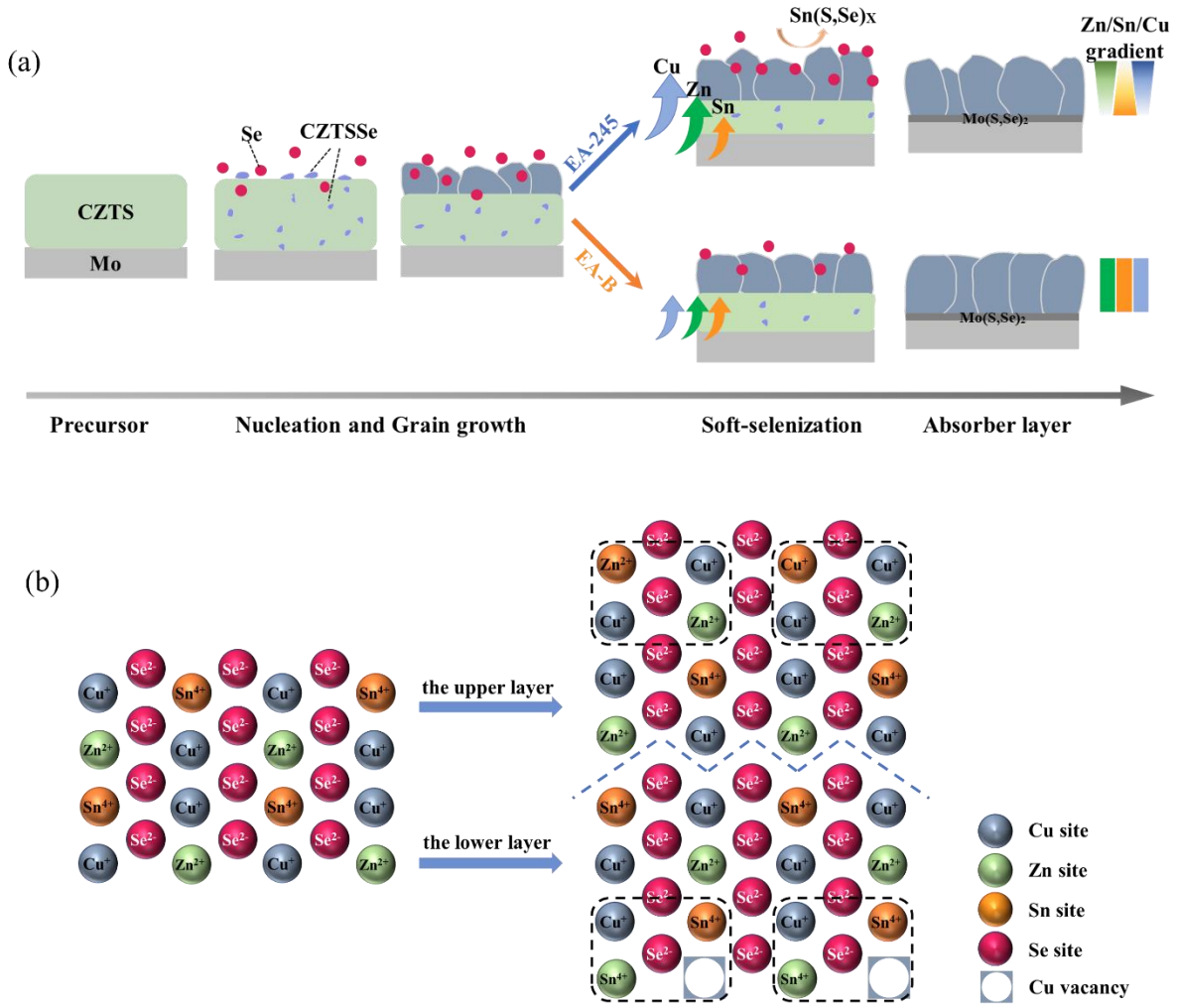

Figure 4. a) Schematic diagram of element distribution and film morphology during the seleniation process. b) The schematic atomic coordination of the EA-245 absorber.

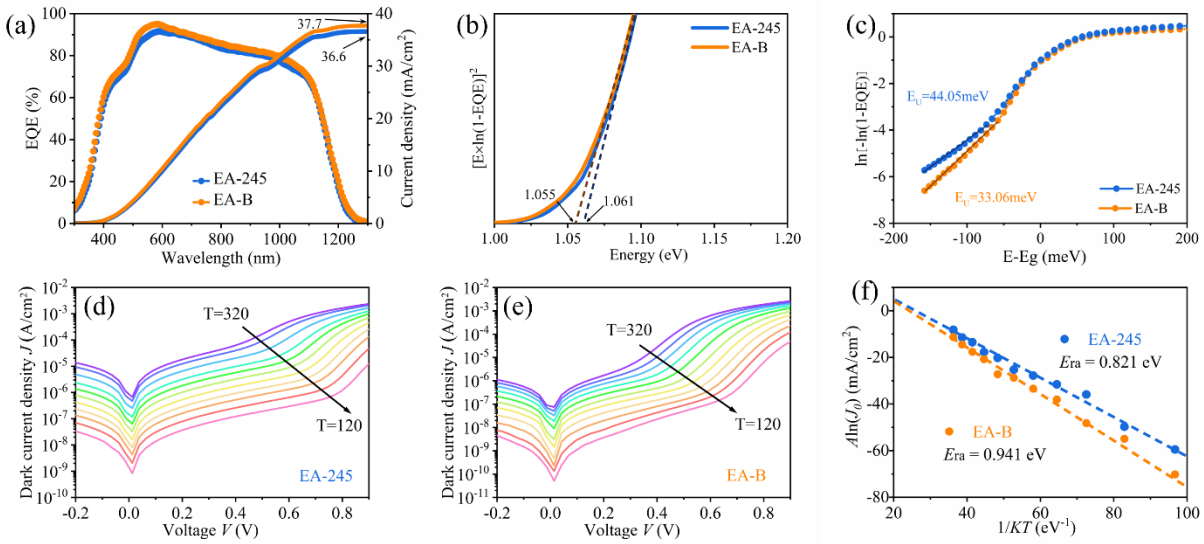

Figure 5. a) EQE spectra and integrated J_{SC} of the champion EA-245 and EA-B devices. b) E_g and c) Urbach energy extracted from the EQE result. The temperature-dependent dark state J-V curves of d) EA-245 device and e) EA-B device. f) the temperature-dependent curve of Aln (J_0) versus $1\cdot(KT)^{-1}$ of the two devices.

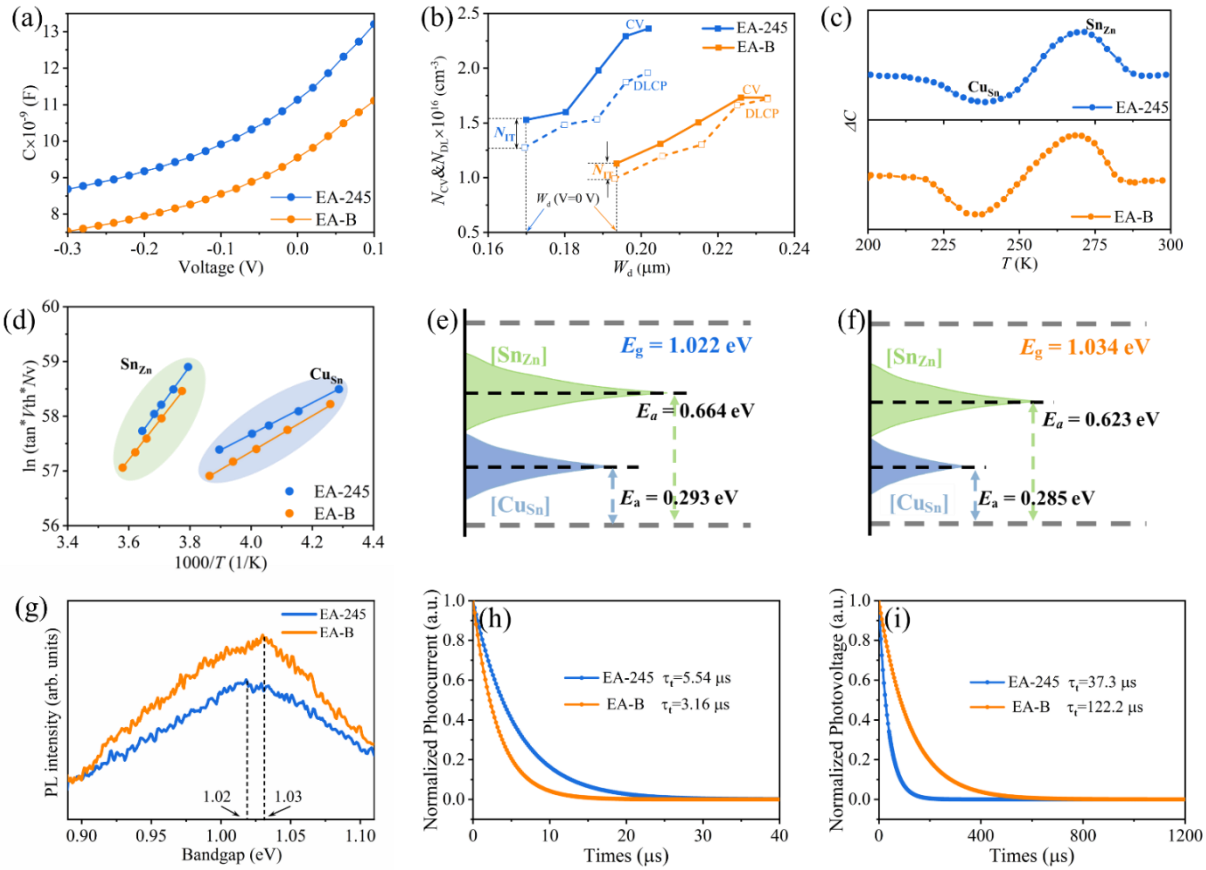

Figure 6. a) C-V curves, b) the profile of C-V and DLCP, c) DLTS spectra, d) Arrhenius curves obtained from DLTS spectra of the EA-245 and EA-B devices. Elementary diagram of the diverse spatial distribution of defects for e) EA-245 device and f) EA-B device. g) PL spectra, h) Normalized TPC spectra of, and i) Normalized TPV spectra for EA-245 and EA-B devices.

Table 4. Summary of relevant parameters of C-V and DLCP measurements.

Sample	RMS [nm]	N_{CV} [cm^{-3}]	N_{DL} [cm^{-3}]	Interface state response (relative values)	W_d [μm]
EA-245	81	1.53×10^{16}	1.28×10^{16}	2.5×10^{15}	0.170
EA-B	67	1.13×10^{16}	0.99×10^{16}	1.4×10^{15}	0.194

Table 5. Activation energy (E_a) and concentrations (N_T) of different defects in CZTSSe solar cells.

Sample	Possible defect level	Activation energy E_a [eV]	Trap concentration N_T [cm^{-3}]
EA-245	Cu_{Sn}	0.293	2.81×10^{14}
	Sn_{Zn}	0.664	1.77×10^{14}
EA-B	Cu_{Sn}	0.285	1.97×10^{13}
	Sn_{Zn}	0.623	1.64×10^{13}

Segmented Control of Selenization Environment for High-Quality $Cu_2ZnSn(S,Se)_4$ Films Towards Efficient Kesterite Solar Cells

Yue Jian[1,2,3], Litao Han[1,], Xiangrui Kong[1], Tianliang Xie[1], Dongxing Kou[1], Zhengji Zhou[1], Shengjie Yuan[1], Guangxing Liang[2,*], Xianghua Zhang[3], Zhi Zheng[4] and Sixin Wu[1,*]*

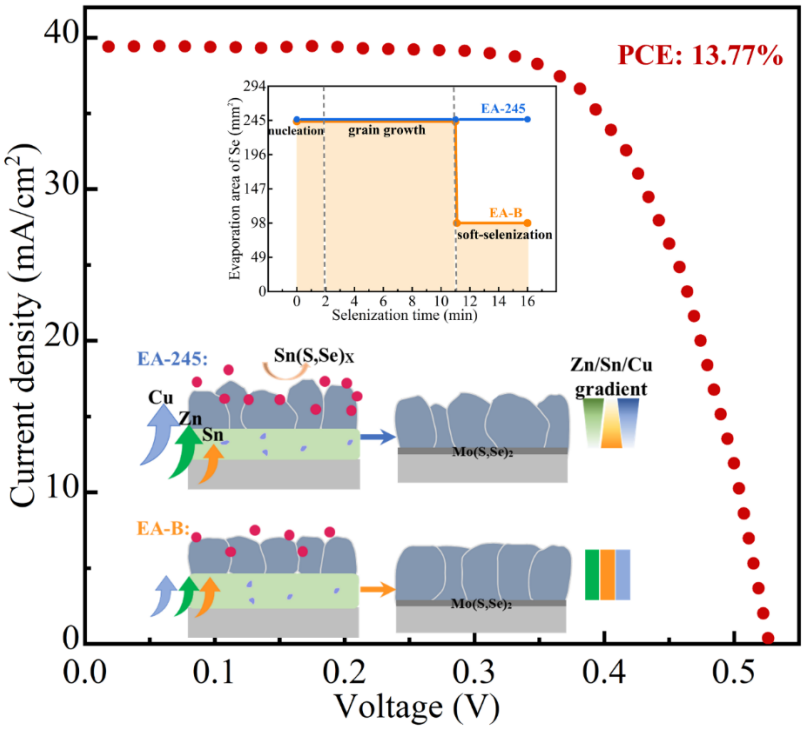

A novel segmented control strategy for selenization environment is introduced to regulate the selenization reaction by controlling the evaporation area of Se. This selenization method helps to promote the element homogenization, optimize surface smoothness, and obtain a high-crystalline-quality absorber with low point defects. And the CZTSSe solar cell with PCE of 13.77% is successfully achieved.